CeO_2–Co_3O_4–CuO anode for direct utilisation of methane or ethanol in solid oxide fuel cells

Sarruf, Bernardo; Hong, Jong-Eun; Steinberger-Wilckens, Robert; Miranda, Paulo Emilio

DOI:
10.1016/j.ijhydene.2018.01.192

Document Version
Peer reviewed version

Citation for published version (Harvard):
Sarruf, B, Hong, J-E, Steinberger-Wilckens, R & Miranda, PE 2018, 'CeO_2–Co_3O_4–CuO anode for direct utilisation of methane or ethanol in solid oxide fuel cells', *International Journal of Hydrogen Energy*, vol. 43, no. 12, pp. 6340-6351. https://doi.org/10.1016/j.ijhydene.2018.01.192

CeO_2-Co_3O_4-CuO anode for direct utilisation of methane or ethanol in solid oxide fuel cells

Bernardo J. M. Sarruf[a,b,*], Jong-Eun Hong[c], Robert Steinberger-Wilckens[b], Paulo Emílio V. de Miranda[a]

[a]*Hydrogen Laboratory COPPE, Metallurgical and Materials Engineering, Federal University of Rio de Janeiro - 21942-971 Rio de Janeiro, RJ, Brazil. Phone:+55 21 3938-8791*
[b]*Centre for Fuel Cell and Hydrogen Research - School of Chemical Engineering, University of Birmingham Edgbaston, Birmingham, West Midlands B15 2TT, UK. Phone:+44 121 415 8169*
[c]*Fuel Cell Laboratory - Korea Institute of Energy Research 152, Gajeong-ro, Yuseong-gu, Daejeon 34129, South Korea. Phone: +82-42-860-3527*

Abstract

The present work aims at producing an electrocatalyst suitable to be used as anode in solid oxide fuel cells that operates with hydrocarbons or alcohols as fuels. A cerium-cobalt-copper anode was developed, characterised and tested with hydrogen, anhydrous methane or anhydrous ethanol as fuels.

The produced catalysts were characterised by X-ray and thermogravimetric analysis as well as H_2 temperature-programmed reduction and post oxidation. For electrochemical performance, i-V curves were taken in different test rigs, guaranteeing reproducibility. Additionally, electrochemical impedance spectroscopy was performed in order to determine cell's polarisation effects. *Post-mortem* analysis was done to assess carbon by Raman spectroscopy and temperature-programmed oxidation. Microstructure images were obtained by scanning electron microscopy.

The cells have shown the ability to operate with hydrogen, methane, or ethanol with high performance. Negligible carbon was found in the *post-mortem* assessment after 24 hours operation. Therefore, the multilayer anode showed to be promising for the direct utilisation of carbonaceous fuels.

Keywords: Solid oxide fuel cells, anodes, coke-resistant anode, anhydrous methane, anhydrous ethanol

[*]Corresponding author Email address: sarruf@labh2.coppe.ufrj.br (Bernardo Jordão Moreira Sarruf)

1.Introduction

Reforming of hydrocarbons is a process widely used in the industry to convert (predominately) natural gas into syngas for further hydrogen production or purification, or as a chemical raw product. Techniques such as steam and dry reforming, shown in Equations 1 and 2, respectively, are applied for methane conversion into hydrogen and carbon monoxide by using a nickel or copper catalyst [1].

$CH_4 + H_2O = CO + 3H_2$, $\Delta H = +206\ kJ.mol^{-1}$ (1)

$CH_4 + CO_2 = 2CO + 2H_2$, $\Delta H = +247\ kJ.mol^{-1}$ (2)

Catalytic partial oxidation is another reaction path used to produce hydrogen and carbon monoxide - if partial oxidation may occur - as well as carbon dioxide when total oxidation takes place. However, the oxidation of methane occurs by an electrochemical route when it is promoted by O^{2-} ions supplied by, for example, a solid oxide fuel cell (SOFC). Equations 3 and 4 show the reaction processes of partial and total electrochemical oxidation, respectively [2].

$CH4 + O^{2-} = CO + 2H_2 + 2e^-$, $\Delta H = -36\ kJ.mol^{-1}$ (3)

$CH_4 + 4O^{2-} = CO_2 + 2H_2O + 8e^-$, $\Delta H = -802\ kJ.mol^{-1}$ (4)

Considering the electrochemical oxidation as a viable path when using an electrochemical converter device such as an SOFC, the “natural” production of steam and carbon dioxide indicated in Equations 3 and 4 must be considered as well. Therefore, internal reforming of the hydrocarbon fuel will be facilitated even though the feeding operation is being held under anhydrous conditions and is initially a purely electrochemical process.

Since the products of thermal decomposition of anhydrous ethanol at 750˚C in an SOFC are mainly hydrogen, carbon oxides, and methane, the electrochemical oxidation will also take place

by means of the decomposition of these products as shown in Equations 5 and 6 in addition to the Equations for methane oxidation and reforming (Equations 1-4).

$$H_2 + O^{2-} = H_2O + 2e^- \quad (5)$$

$$CO + O^{2-} = CO_2 + 2e^- \quad (6)$$

Yet, for ethanol decomposition the eventual production of ethane and ethylene should be considered. The thermal decomposition of ethane and ethylene are events that should be avoided as it leaves carbon adsorbed over the catalyst surface, as shown in Equations 7 and 8.

$$C_2H_6 = 3H_2 + 2C \quad (7)$$

$$C_2H_4 = 2H_2 + 2C \quad (8)$$

However, instead of promoting the decomposition of ethane and ethylene, the electrochemical oxidation of these by-products is also feasible as shown in Equations 9 and 10 [3].

$$C_2H_6 + 3.5O^{2-} = 2CO_2 + 3H_2O + 7e^- \quad (9)$$

$$C_2H_4 + 6O^{2-} = CO_2 + 2H_2O + 12e^- \quad (10)$$

Nickel-based anodes have shown to work as state-of-the-art catalyst, for hydrogen and for hydrocarbon fuels. However, these materials are prone to carbon depletion [4, 5] that is a well-known phenomenon caused by the massive coking, which deactivates the catalyst and clogs the fuel stream. Ceria-based anodes, especially those with copper addition in their composition, have been showing interesting results for the use with hydrocarbon and alcohol fuels directly converted in SOFCs, avoiding coking. Cerium oxide, as a mixed ionic electronic conductor (MIEC), has shown to be a suitable material for the electrocatalytic oxidation of hydrocarbon fuels whereas copper presents the ability of preventing coking over the catalyst surface and increasing electronic conductivity of the anode [3, 6-8].

This work addresses the development of a multifunctional ceria-cobalt-copper anode for the use of methane or ethanol as direct fuel in their anhydrous form in an SOFC anode chamber. The

main objective is to work within a catalyst capable of performing electrochemical oxidation of hydrocarbons and alcohols via O^{2-} as seen, for instance, in Equations 9 and 10. Additionally, since the production of steam and carbon oxides are inevitable, these could be used to promote fuel internal reforming and henceforth have the overall electrochemical/chemical efficiency of the process enhanced.

2.Experimental

Firstly, two bimetallic ceria-based electrocatalyst materials were synthesised by the amorphous citrate method. The former composition with a molar proportion of Ce:Co:Cu - 2:1:1, and the latter with a proportion 1:2:1. The details of the amorphous citrate synthesis method are described in one of our previous papers [7]. The two different powders were characterised by X-ray diffraction (XRD) using a Bruker D8 diffractometer varying 2θ from 10 to 90˚ in steps of 0.02˚ with a CuKα = 0.15418 nm radiation source. XRD analysis was done on the as-synthesised powder and after annealing it at 800˚C during two hours to observe phase crystallisation. Rietveld refinement was applied to the X-ray raw data using the FullProf Suite software in which the background was described by a linear interpolation of pre-determined points with refinable heights.

Thermogravimetric analysis was performed to determine the volatile's evaporation temperature as well as eventual oxide decomposition. A NETZSCH TG 209 F1 was used ranging from room temperature to 900˚C with a 10 ˚C.min^{-1} heating rate and 30 minutes dwelling at 900˚C in air.

Temperature-programmed reduction - TPR - was performed on the powders after the annealing treatment to test the reducibility of each compound. A Quantachrome ChemBET Pulsar TPR/TPD unit was used for this with approximately 20 mg of catalyst powder in a quartz reactor that heated from room temperature to 900˚C in 10 ˚C.min^{-1} steps. The reducing gas mixture consisted of 5% hydrogen in balanced nitrogen. H_2-TPR/TPO cycles were done to assess for reducing behaviour of each powder. Previously to the first TPR profile, the sample was kept at 500˚C under oxygen-rich atmosphere during at least 30 minutes to assure full oxidation. After oxidation treatment, TPR was performed as aforementioned, followed by oxygen injections of 50 μL at 500˚C. The injections were done until the break-through point was attained. Finally, a

second cycle, TPR + oxygen pulses, was done for comparison and discussion about eventual phases evolution.

After powder characterisation, single cells were assembled using scandia and ceria-doped zirconia (ScCeSZ) electrolyte supports HIONIC from Fuel Cell Materials, around 150 μm-thick onto which an interface layer composed by CeO_2 and ScCeSZ (50% wt.) was screen printed and sintered at 1300˚C for three hours. This interface layer was deposited to mitigate thermal mismatch effects between anode and electrolyte. Thermal coefficients for the oxides can be found elsewhere [9-12]. A lanthanum strontium-doped manganite (LSM) cathode was then screen printed and sintered at 1100˚C for two hours on the other side of the electrolyte. The first layer of the actual anode (Ce:Co:Cu - 2:1:1) was deposited by screen printing with electrode active area of approximately 1 cm^2, over the interface layer and dried at 150˚C for 30 minutes. Following this, the last layer of the anode (Ce:Co:Cu - 1:2:1) was screen printed over the former and the ensemble was calcined at 900˚C for two hours. Silver wires, pasted with silver ink, served as current collectors.

Electrochemical tests consisting of i-V curves were performed whilst the cathode was fed with pure oxygen as oxidant and the anode with hydrogen, anhydrous methane, or anhydrous ethanol as fuels. For tests with hydrogen and methane, the fuel was added directly into the anode chamber whereas for ethanol testing, the fuel stream was filled with ethanol vapour carried with nitrogen. Tests were performed over two cells and ran on two different test rigs; the former at the University of Birmingham, and the latter at the Federal University of Rio de Janeiro, to confirm reproducibility. Additionally, electrochemical impedance spectra were recorded when hydrogen, methane and ethanol were fed individually to the cells. Frequency ranged from 1 MHz to 50 mHz at open circuit voltage and amplitude current of 10 mA.

Post-mortem analysis was carried out to assess carbon deposition on the anode both by Raman spectroscopy and temperature-programmed oxidation - TPO. Raman spectroscopy was done with a 633 nm wavelength laser in a Renishaw inVia Raman microscope. Samples were scanned from 3200 to 100 cm^{-1} with an acquisition time of 20 seconds and 1% of the laser total power. An operated cell was put in a quartz tube reactor under oxidising atmosphere inside a tubular furnace that varied from 150 to 850˚C whilst the outlet oxidised products were analysed

by the gas cromatograph, quantifying eventual carbon oxides formed. In addition, SEM/EDX analysis was performed on a sample of an anode that was reduced and aged for 50 hours at 800˚C in a hydrogen-rich atmosphere. EDX images were treated with noise filters such as mean and median and the position of the cations was estimated and displayed in one single merged image using Matlab.

3.Results and Discussion

3.1. Powder Characterisation

Figure 1 shows the X-ray pattern for the synthesised powders. The red dashed lines represent the data for the powders as-synthesised whilst the continuous black line represent the pattern for each powder after heat treatment at 800˚C. The peaks become narrower and sharper after heat treatment indicating phase crystallisation. The binary phase diagrams of CeO_2, Co_3O_4 and CuO indicate that the oxides are expected to be formed as isolated phases [13-16].

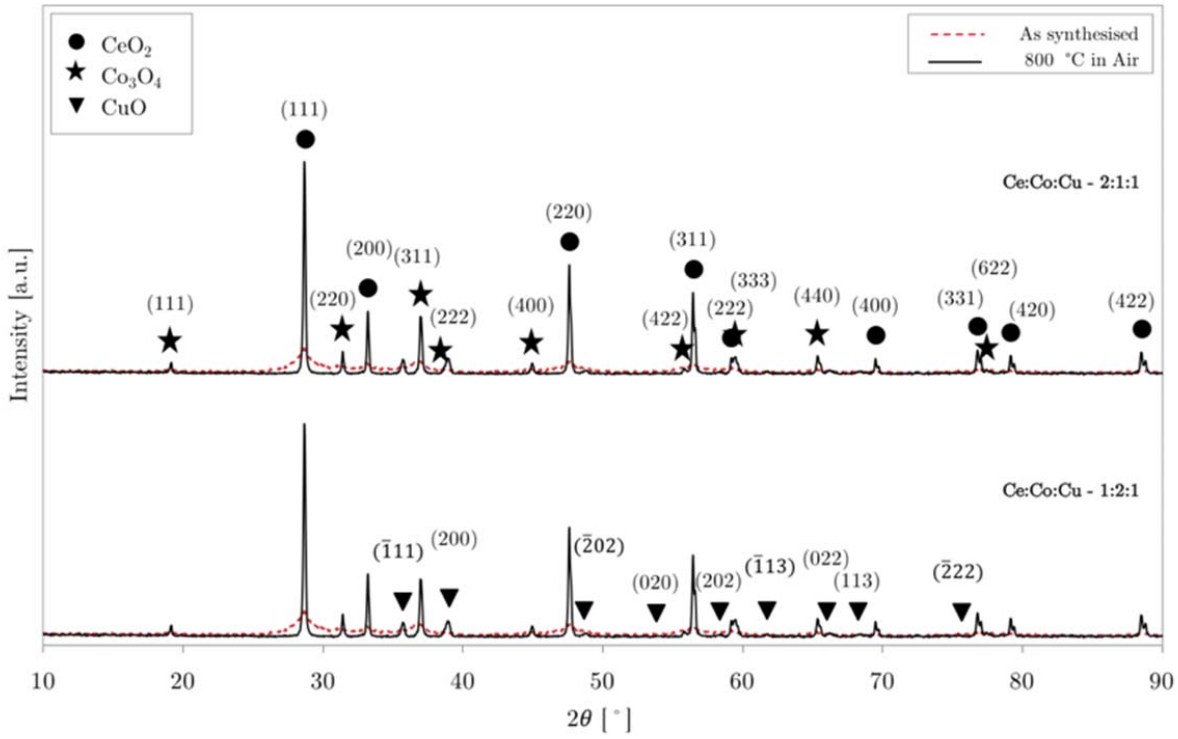

Figure 1: X-ray pattern for the as-synthesised and heat-treated powder.

Rietveld refinement was performed over the raw data of the crystallised powders and the results are shown in Table 1. The refinement was done considering PDF-03-065-2975, PDF-00-042-1467 and PDF-04-007-1375 for CeO_2, Co_3O_4 and CuO, respectively, as a start for the iteration process. From the PDF cards, CeO_2 has the cubic structure of fluorite with symmetry space group Fm-3m whereas Co_3O_4 is a cubic spinel from space group Fd-3m and CuO has the monoclinic tenorite structure and space group C 2/c.

The lattice parameters calculated slightly deviate from the theoretic values taken from PDF cards. However, literature shows that Ce-Cu solid solutions are most likely not to occur [15, 17]. On the other hand, cobalt has solubility into the ceria lattice [16, 20], but no solid solution between these metals were found by X-ray analysis in this work.

Table 1: Lattice parameters for the oxides - Rietveld refinement.

Compositions	Oxide	Structure	Space Group	a [nm]	b [nm]	c [nm]	α [°]	β [°]	γ [°]	Coeff.

Cerium-rich	CeO_2	Fluorite	Fm-3m	0.5409(5)	0.5409(5)	0.5409(5)	90.00	90.00	90.00	Rp=27.8%
	Co_3O_4	Spinel	Fd-3m	0.8074(6)	0.8074(6)	0.8074(6)	90.00	90.00	90.00	Rw=15.6%
	CuO	Tenorite	C 2/c	0.4696(4)	0.3408(0)	0.5127(5)	90.00	99.66	90.00	$\chi^2 = 1.14$
Cobalt-rich	CeO_2	Fluorite	Fm-3m	0.5411(4)	0.5411(4)	0.5411(4)	90.00	90.00	90.00	Rp=33.3%
	Co_3O_4	Spinel	Fd-3m	0.8079(0)	0.8079(0)	0.8079(0)	90.00	90.00	90.00	Rw=16.9%
	CuO	Tenorite	C 2/c	0.4698(4)	0.3410(5)	0.5132(1)	90.00	99.66	90.00	$\chi^2 = 1.04$

In Figure 2 the results of thermogravimetric analysis for both cerium-rich and cobalt-rich powders are presented. As can be seen inserted in the graphs the first losses for both compositions occurred from 25 to 450˚C and represent 5.77 and 5.44 % for the cerium and cobalt-rich compositions, respectively. Those are probably due volatile evaporation and compounds oxidation originated from synthesis process, such as water and nitrates.

The second mass loss occurred from 850˚C onwards for both compositions and can be assigned to cobalt oxide decomposition as in Equation 11. Cobalt oxide decomposition shows an oxygen mass loss of around 7% from Co_3O_4 to CoO. Considering the CeO_2-Co_3O_4-CuO mixture the cobalt oxide decomposition represents a theoretical oxygen loss of 1.09 and 2.71% for cerium and cobalt-rich compositions, respectively which are in fair accordance with the experimental TGA results of 0.86 and 2.41% shown in Figures 2a and 2b, respectively measured from 850˚C onwards.

$$2CO_3O_4 = 6CoO + O_2 \quad (11)$$

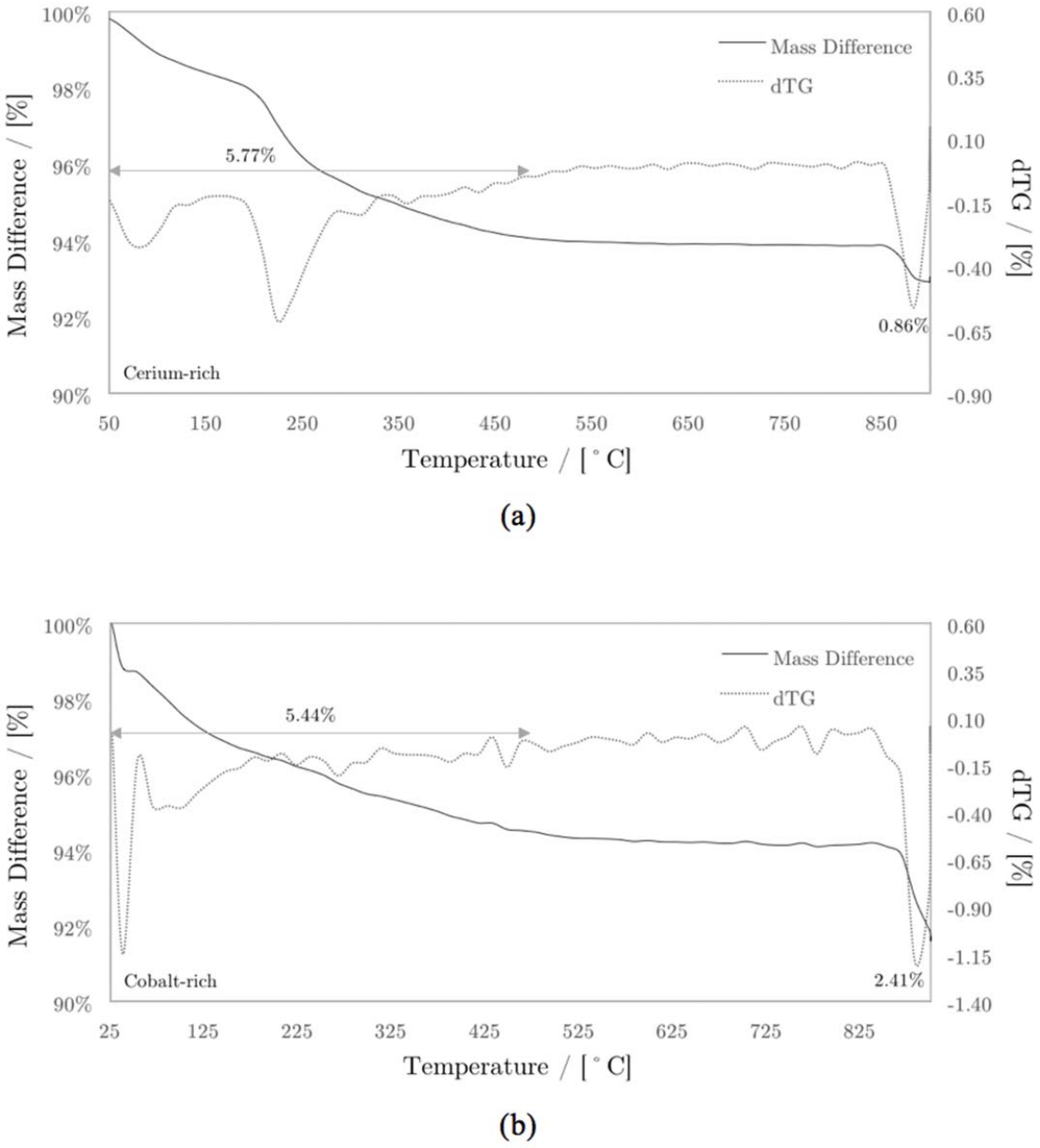

Figure 2: Thermogravimetric analysis of (a) Cerium-rich and (b) Cobalt-rich powder compositions.

The results of H_2-TPR are shown in Figure 3. Since each powder is composed of a mixture of oxides, the peaks of hydrogen consumption overlap and were, thereby, deconvoluted. The reduction of copper oxide as isolated phase usually takes place between 150 and 500˚C according to Equations 12 and 13 [19-21].

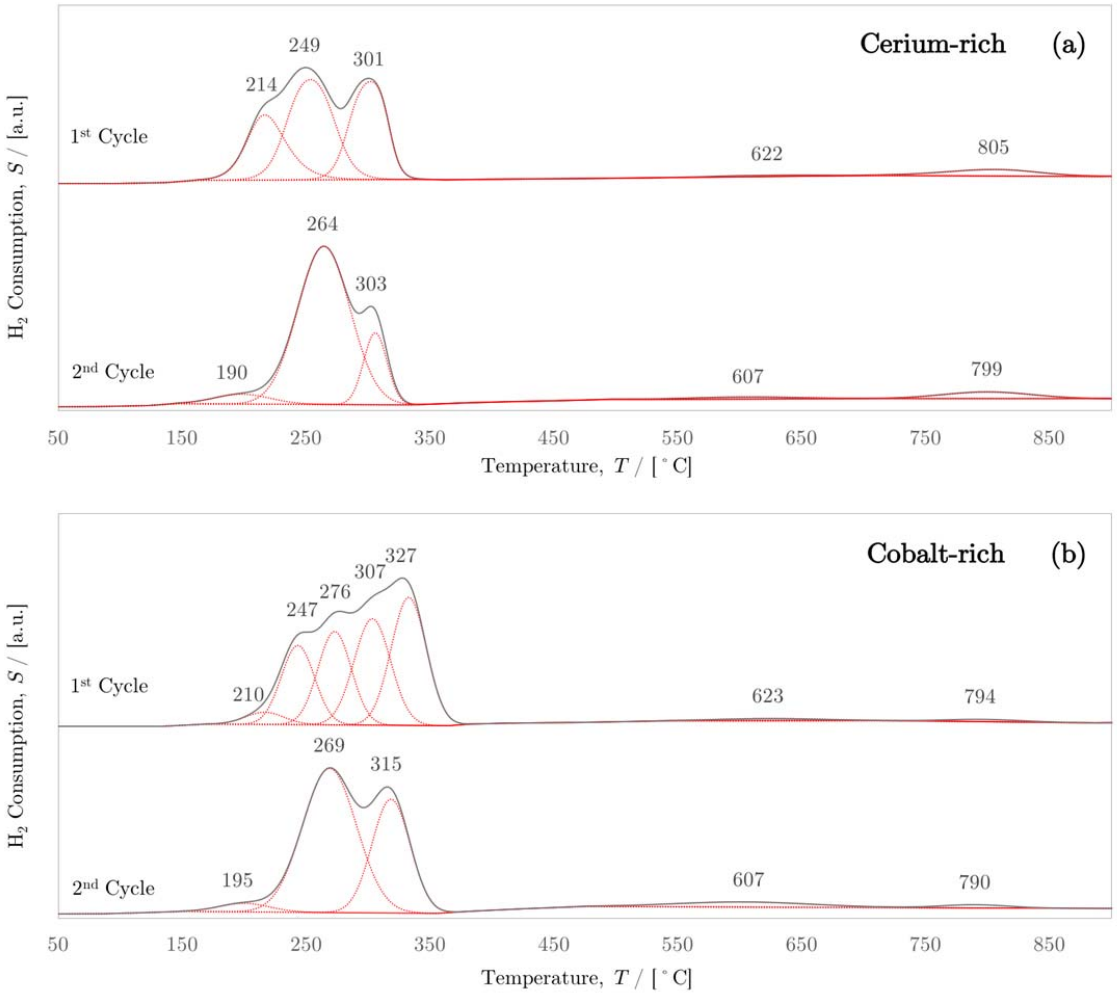

Figure 3: Temperature-programmed reduction cycles after full oxidation of the cerium-rich and the cobalt-rich powders.

Cobalt oxide, analogously to copper oxide, reduces in two steps. The first reducing reaction occurs according to Equation 14 around 300˚C for the cobalt oxide whereas total reducing will take place around 500˚C as depicted in Equation 15 [22, 23].

$$2CuO + H_2 = Cu_2O + H_2O \quad (12)$$

$$Cu_2O + H_2 = 2Cu + H_2O \quad (13)$$

$$Co_3O_4 + H_2 = 3CoO + H_2O \quad (14)$$

$$CoO + H_2 = Co + H_2O \quad (15)$$

The profile, shown in Figure 3b, demonstrates high activity from 300-330˚C in the first cycle, thereby this can be assigned for cobalt oxide full reduction, since this is a cobalt-rich sample. However, in the second cycle for the same sample, peaks became broader and the superposing effect could not be well-defined. This is due slight sintering of the metallic particles, especially copper, at high temperatures such as 900˚C. Coarsening of particles reduces available surface area thus making them more resistant to reduction or less active. However, since the temperature profile does not move significantly towards higher temperatures, it is concluded that the catalyst did not suffer higher levels of coarsening after two redox cycles even at critical temperatures such as 900˚C.

Regarding cerium oxide, the reducing process is defined by the peaks at higher temperatures. The reduction of CeO_2 will occur partially, turning Ce^{4+} into Ce^{3+} as shown in Equation 16. The cerium oxide lattice will become oxygen-deficient as reduction takes place, thus enhancing the electrical conductivity of this phase. Moreover, the cerium oxide reduction process occurs also in two well-defined steps. Firstly, the surface-capping oxygen anions attached to the Ce^{4+} surface with an octahedral coordination will react with hydrogen at temperatures such as 500 to 650˚C, depending on the particle size distribution. Then finally oxygen from ceria's bulk structure will be released at temperatures above 750˚C [19, 20, 24]. Analysing the reduction profile of the oxide powders it is reasonable to conclude that the anode material can be properly activated at temperatures such as 700-750˚C under hydrogen atmosphere.

$$2CeO_2 + H_2 = 2CeO_{1.5} + H_2O \quad (16)$$

H_2-TPR results have shown the ability of the oxides to absorb hydrogen and be easily reduced into metals that may fully work as catalyst and as electrical percolated contact regarding cobalt and copper, respectively. Although cobalt and copper oxides are most likely to be reduced into metals, ceria will probably be reduced to CeO_{2-x} thus presenting lack of oxygen which polarises the structure and enhances conductivity. It is also known that depending on ceria's particle size, this oxide may have its oxygen storage capacity (OSC) enhanced due to the oxygen under-stoichiometry over the surface of ceria [25]. Yet, for both samples, cerium-rich and cobalt-rich, it is notable that cerium oxide reducing temperatures remain unaltered after each cycle.

Table 2: Hydrogen/Oxygen consumed after each cycle for both catalysts

Cycles	Consumption		Cerium-rich	Cobalt-rich
First Cycle	Hydrogen consumption	[mmols.g^{-1}]	5.7	11.2
		[mL.g^{-1}]	127.6	250.7
	Oxygen uptake	[mmols.g^{-1}]	2.9	5.1
		[mL.g^{-1}]	64.9	113.9
Second Cycle	Hydrogen consumption	[mmols.g^{-1}]	5.8	9.8
		[mL.g^{-1}]	130.4	219.9
	Oxygen uptake	[mmols.g^{-1}]	2.9	5.4
		[mL.g^{-1}]	66.1	121.0

Furthermore, the amount of hydrogen and oxygen absorbed during reducing/oxidation cycles were calculated and are displayed in Table 2. It can be noticed that cobalt-rich catalyst absorbs more hydrogen, since this composition has more metallic phase available. Additionally, the ratio between H_2/O_2 consumed at each cycle is close to 2, which is consistent to what it would be expected from Equation 17. Also, the reduction of cobalt and copper oxides occur at similar ranges for both samples and cycles – approximately from 200 to 350˚C – thus indicating that the ability to undergo reduction does not change drastically between these two catalysts.

$$H_2 + 0.5O_2 = H_2O \quad (17)$$

Another point worth noting is how the second cycles for both powders becomes very similar, with one sole big difference in peaks at 303 and 315˚C for cerium-rich and cobalt-rich sample, respectively. This increased area of the peak at 315˚C for the latter, clearly indicates the reduction of cobalt oxides at this point, since the presence of cobalt is higher within this sample.

3.2. Electrochemical performance of cells

Figure 4 shows the maximum power density and open circuit voltage (OCV) for two cells fabricated (SOFC#1 and #2), and operated on hydrogen, methane and ethanol as fuels. In Figure 4a the tests with hydrogen at 750, 800 and 850˚C have shown power densities of 137, 260 and 411 mW.cm^{-2} and current densities at 0.7 V were 181, 340 and 518 mA.cm^{-2}, respectively. These

results were reproducible when tested at 700, 750 and 800˚C with a replica (SOFC#2). Figure 4b shows power densities such as 101, 156 and 260 mW.cm^{-2} with hydrogen as fuel. Moreover, the current densities at 0.7 V for these conditions were 128, 226 and 385, mA.cm^{-2}, respectively.

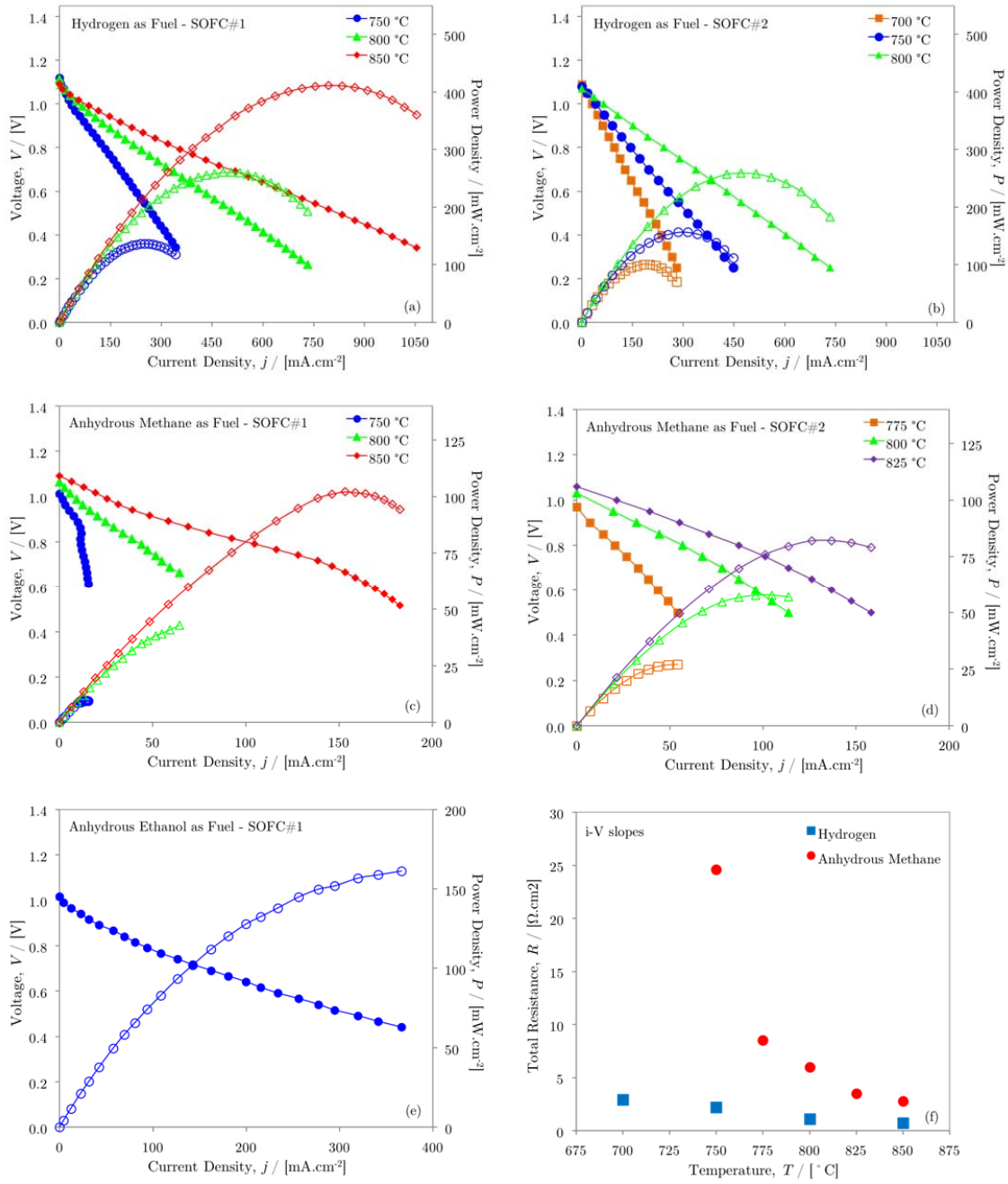

Figure **4:** i-V plots for (a) SOFC#1 and (b) SOFC#2 both with hydrogen as fuel, (c) SOFC#1 and (d) SOFC#2 with anhydrous methane as fuel (e) SOFC#1 with anhydrous ethanol and (f) the calculated slopes of hydrogen and methane i-V curves.

The results of using anhydrous methane as fuel, are shown in Figures 4c and 4d. The power densities for the first cell tested were 10, 43 and 95 $mW.cm^{-2}$ whereas current densities at 0.7 V were 14, 59 and 146 $mA.cm^{-2}$ at 750, 800 and 850˚C, respectively. For the replica, cell results were 27, 58 and 82 $mW.cm^{-2}$ for power densities and as for current densities at 0.7 V, 33, 78 and 115 $mA.cm^{-2}$ at 775, 800 and 825˚C.

It must be highlighted that these two sets of tests were performed with two cells in different test rigs at two different facilities. Therefore, the results have shown fair reproducibility for this material and the manufacturing procedures applied. Moreover, Figure 4e shows results obtained with anhydrous ethanol as fuel that delivered over 161 $mW.cm^{-2}$ of power density and an OCV of 1.02 V at 850˚C. The current density at 0.7 V was 180 $mA.cm^{-2}$.

Figure 4f shows the calculated slopes of the i-V curves where the total resistance of the cells is estimated for hydrogen and methane as fuels. The resistances will be discussed after the impedance results are shown. The power densities, open circuit voltage (OCV) values as wells as the i-V slopes have been compiled in Table 3.

Table 3: Results of i-V plot testing for cells SOFC#1 and SOFC#2.

Fuel	Temperature [˚C]	Max. P. Density [$mW.cm^{-2}$]		OCV [V]		Slopes i-V [$\Omega.cm^2$]
		SOFC#1	SOFC#2	SOFC#1	SOFC#2	
Hydrogen as Fuel	700	---	101	---	1.09	2.90
	750	137	156	1.12	1.08	2.00
	800	260	259	1.11	1.07	1.10
	850	411	---	1.09	---	0.70
Anhydrous Methane	750	10	---	1.01	---	24.60
	775	---	27	---	0.97	8.50
	800	43	58	1.06	1.03	6.00
	825	---	82	---	1.06	3.50
	850	95	---	1.09	---	2.80
Anhydrous Ethanol	850	161	---	1.02	---	1.50

The spectra of electrochemical impedance can be seen in Figure 5. After the tests were done, the fitting of the raw data points was performed with Z-View 3.2b software. The element circuit

model (ECM) utilised was a resistance R1 in series with two parallel RQ (resistance and constant phase element) R2Q1 and R3Q2. The dataset is represented in all spectra as open symbols whereas the fitting model are continuous line. Figure 5a, shows spectra taken at 750˚C with hydrogen and anhydrous methane as fuels. The structure of both spectra is very similar, with two arcs described by elements R2Q1 and R3Q2. In Figure 5b, both fuel tests are represented for tests performed at 800˚C whereas in Figure 5c are the tests with hydrogen, methane and ethanol at 850˚C.

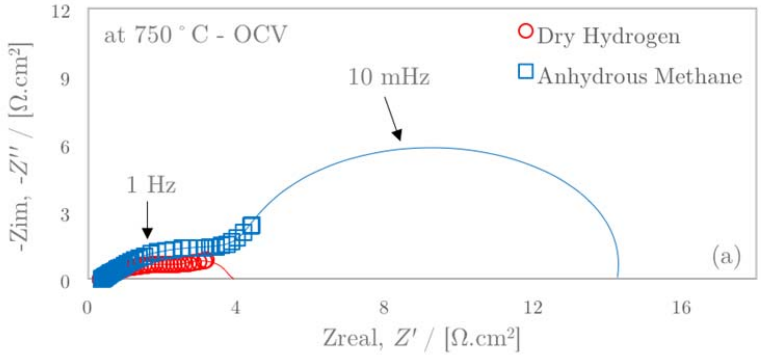

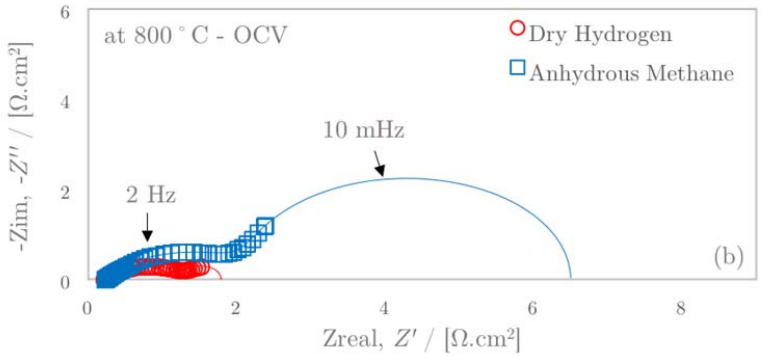

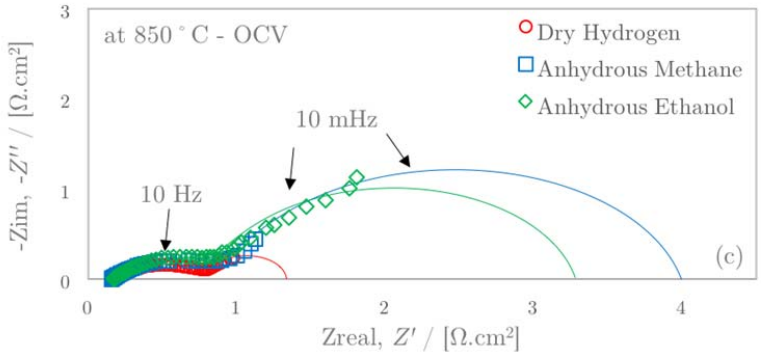

Figure **5:** Nyquist plots of impedance spectra with hydrogen and anhydrous methane (a) at 750˚C, (b) 800˚C and with hydrogen, methane and anhydrous ethanol (c) at 850˚C.

Table 4 summarises the calculated results of Ohmic resistance and total polarisation which are the first and last real axis values crossing the imaginary axis at 0, respectively. It is important to highlight the behaviour of the Ohmic resistance with increasing temperature, as seen in Table 4, for all fuel condition, which is consistent with a 150 μm-thick electrolyte support. In addition, the results of total polarisation are also in agreement with the slopes from i-V curves, which can be seen in Table 3.

Table 4: Polarisation resistances with cell at various temperatures with hydrogen, methane and ethanol as fuels.

Fuel	Temperature [˚]	Ohmic Resistance [$\Omega.cm^2$]	Polarisation [$\Omega.cm^2$]	Total Polarisation [$\Omega.cm^2$]
Hydrogen	750	0.33	3.58	3.92
	800	0.22	1.58	1.80
	850	0.19	1.15	1.34
Anhydrous Methane	750	0.37	13.90	14.27
	800	0.24	6.26	6.50
	850	0.16	3.84	4.00
Anhydrous Ethanol	850	0.17	3.11	3.28

It is notable that the second arc of the Nyquist plots in Figure 5 become bigger as fuel condition is changed, indicating that this arc is probably referred to the anode polarisations effect. However, the first arc remains almost unaltered thereby showing that it can be assigned to cathode effects, since cathodic feeding conditions were kept steady.

3.3. Post-mortem characterisation

Raman spectra in Figure 6 show peaks located at 196, 482, 523, 621 and 691 cm^{-1} that are related to Co_3O_4 [26-29], 286 and 347 cm^{-1} to CuO [30] and 462 cm^{-1} to CeO_2 [31]. Peak at 550 cm^{-1} is assigned to Cu_2O [32]. The ceria peak at 460 cm^{-1} can be assigned to the CeF_{2g} mode due to symmetrical stretching of the O-Ce-O vibrational unit in octahedral coordination [33, 34]. The absence of a fluorite-type structure at 600 cm^{-1} suggests that solid solutions were less likely formed [32] which corroborates with the previous X-ray discussion. In addition, broadening and

shifting of the CeF_{2g} band indicates that ceria's particle size might have changed [28].

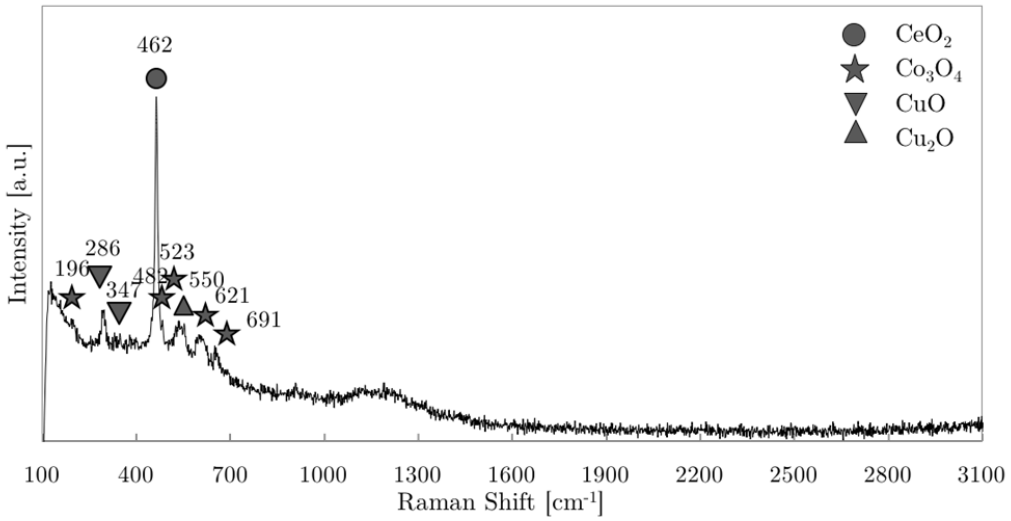

Figure 6: Raman spectroscopy of the cell operated with anhydrous methane.

The Raman peaks of crystalline Co_3O_4 are related to E_g (482 cm^{-1}), F_{2g} (523 and 621 cm^{-1}) and A_{1g} (691 cm^{-1}) modes [22, 35, 36]. Therefore, this confirms that cobalt oxide is present only in its highest state of oxidation (Co_3O_4) even after the cell being operated. The peaks at 286 and 347 cm^{-1} of CuO can be assigned to the A_g and B_g vibrational modes, respectively [37]. Although peak locations are slightly different from literature (298 and 345 cm^{-1} [38]), this can be due to particle size effects.

The most important result is that no carbon was found over the anode surface. Carbon is usually assigned to 1330, 1580 and 2660 cm^{-1}, referring to G, D and 2D bands, respectively which were not spotted in the Raman spectrum.

The graph in Figure 7 shows the TPO profiles for a sample of 12.55 mg of graphite powder and the anode after being operated with direct methane for over at least 24 hours. The GC coupled to the outlet gas that flowed through each sample could detect the absolute amounts of CO and CO_2 as products of carbon oxidation over a temperature range of 150 to 850˚C.

The graph represents the molar amounts in comparison to the baseline test with carbon black. The sum of the products of oxidation for each composition was done and compared to the

graphite mass previously known. The amounts of carbon oxidised from the anode was estimated as 0.36 mg, and considering the anode average volume (around 1.5×10^{-3} cm^3) it can be said that the carbon deposit was in the order of 0.23 g per cm^3 of anode, representing roughly less than 5% wt. of the anode material mass.

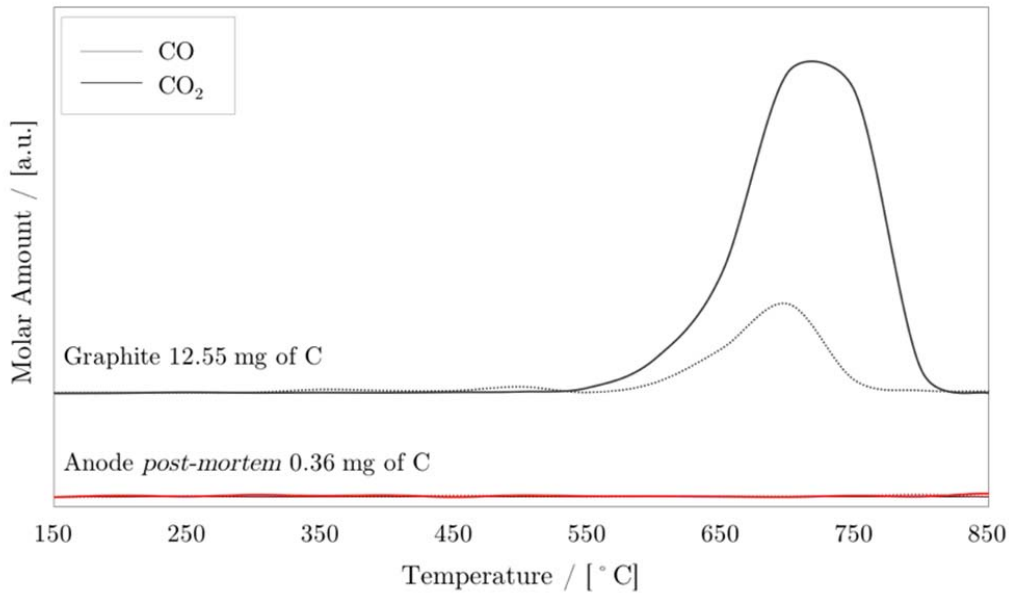

Figure 7: Temperature-programmed oxidation of a known carbon black graphite aliquot and a methane-operated cell.

The results from Raman spectroscopy have shown no carbon over the surface of the anode whereas TPO show negligible carbon formed. Further investigation can be done with long-term experimental to confirm that the amount of built carbon will remain close to the already mentioned results. This will corroborate with the idea that the desired reaction pathways such as electrochemical oxidation and internal reforming were predominant, since any bulky carbon formed was oxidised prior to TPO investigation. However, the results found so far indicate this material as promising for hydrocarbon and alcohol direct utilisation.

The SEM images of the anode/electrolyte interface cross section are shown in Figures 8a and 8b. The microstructure shows reasonable porosity and structural integrity after simulated operation for 50 hours in hydrogen-rich atmosphere. In addition, the sintered microstructure typically shows an interconnected porosity within the cross-section and the tiny particles of the

ceramic material seem to be well adhered amongst each other.

The cross-section image gives an idea of layer thickness considering the buffer layer (CeO_2-ScCeSZr) with a thickness around 6 µm whereas the subsequent anode layers (cerium-rich and cobalt-rich) have a thickness around 9 µm each. The anode structure all together is around 24 µm thereby very thin when compared to the electrolyte support which is around 150 µm.

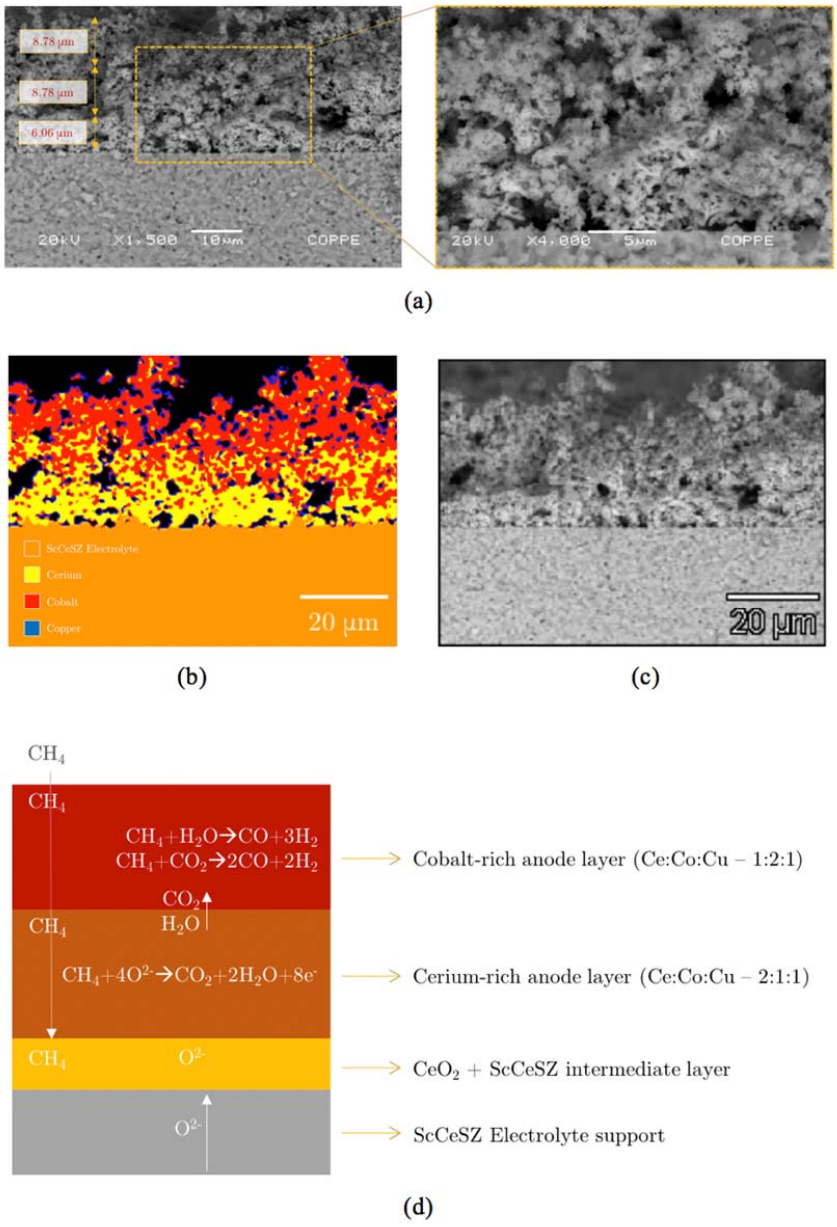

Figure 8: Scanning electron microscopy images showing (a) cross section with anode layer thicknesses, (b) EDX

mapping region of interest, (c) EDX element mapping and (d) the anode layer configuration scheme along with the anode functions.

Scanning-electron images together with the EDX merged images show that the cobalt content through the microstructure increases towards the surface of the anode which was desired when the multifunctional anode was previously designed as shown in Figure 8c.

The proposed reactional mechanism for this anode configuration is shown in Figure 8d. The cerium-rich material, with additions of cobalt and copper near the electrolyte is supposed to promote electrochemical reactions such as those depicted in Equations 3 and 4, whilst cobalt-rich material plays a catalytic role by facilitating internal reforming aided by steam and carbon dioxide inevitably produced by the previous reactions.

Furthermore, the importance of copper on preventing coking is indicated in many works in the literature [39, 40] and it is once more confirmed at the present work. However, the main differences between, Lee et al [39, 40] and the present work is the utilisation of a Ni-free anode, with the insertion ceria-based buffer layer, that aims to enhance adhesion between anode and electrolyte. Electrochemical results have great potential to be enhanced, once electrolyte's thickness is reduced.

Eventually, the migration to anode-supported cell, will increase even more cells performance. The focus of this work so far, was to develop a cell morphology with a ceria-based structure and metal additions that can aid electrochemical oxidation of anhydrous carbonaceous fuels and eventually use the by-products (steam and carbon dioxides) to perform internal reforming as an ideal SOFC.

4. Conclusions

The cerium-cobalt-copper material prepared has shown the ability of operating as SOFC anode with both pure methane and ethanol. In addition, manufacturing procedures and material synthesis have also shown to be reproducible as different cells were tested in different test rig conditions with very similar results.

The electrochemical performance showed a suitable behaviour with hydrogen as fuel

considering a typical benchmark of around 400 $mA.cm^{-2}$ at a potential of 0.7 V. The cells have also shown to be promising for methane or ethanol as fuels. H_2-TPR/O_2 pulse analysis has elucidated how the phases evolution occur at redox conditions and the reactants absorption estimation has confirmed that the reducibility and catalytic activity are kept after samples recycling.

Post-mortem characterisation showed essentially, negligible remaining carbon both by Raman spectroscopy and TPO. Finally, SEM/EDX showed that the microstructure presented enough porosity after ageing and phases were well distributed over the anode cross section.

Acknowledgements

The authors would like to acknowledge the PhD scholarship, granted by the Brazilian National Council for Scientific and Technological Development (CNPq) registered under the grant number 200665/2015-4 and the financial support from BNDES, Oxiteno S.A., and EnergiaH Ltda under grant number 11.2.0323.

References

[1] J. R. Rostrup-Nielsen, Catalytic steam reforming., Catal. Sci. Technol. **5** 1 (1984).

[2] J. Zhu, D. Zhang, K. D. King, Reforming of CH4 by partial oxidation: thermodynamic and kinetic analyses., Fuel **80** 899 (2001).

[3] S. A. Venâncio, P. E. V. Miranda, Direct utilization of carbonaceous fuels in multifunctional SOFC anodes for the electrosynthesis of chemicals or the generation of electricity., Int. J. Hydrog. Energy **42** 13927 (2017).

[4] J. R. Rostrup-Nielsen, J. B. Hansen, D. Helveg, N. Christiansen, A.-K. Jannasch, Sites for catalysis and electrochemistry in solid oxide fuel cell (SOFC) anode., Appl. Phys. A **85** 427 (2006).

[5] C. Schluckner, V. Subotić, V. Lawlor, C. Hochenauer, CFD-simulation of effective carbon gasification strategies from high temperature SOFC Ni–YSZ cermet anodes, Int. J. Hydrog. Energy **42** 4434 (2017).

[6] X.-F. Ye, S. R. Wang, Q. Hu, J. Y. Chen, T. L. Wen, Z. Y. Wen, Improvement of Cu-CeO_2 anodes for SOFCs running on ethanol fuels., Solid State Ion. **180** 276 (2009).

[7] S. A. Venâncio, P. E. V. Miranda, Synthesis of $CeAlO_3$/CeO_2-Al_2O_3 for use as a solid oxide fuel cell functional anode material., Ceram. Int. 37 3139 (2011).

[8] A. Fuerte, R. X. Valenzuela, M. J. Escudero, L. Daza, Study of a SOFC with a bimetallic Cu–Co–ceria anode directly fuelled with simulated biogas mixtures, Int. J. Hydrog. Energy, **39** 4060 (2014).

[9] L. Kundakovic, M. Flytzani-Stephanopoulos, Cu- and Ag-Modified Cerium Oxide Catalysts for Methane Oxidation., J. of Catalysis, 179 203 (1998).

[10] P. Wang, J. Zhang, Y. Bai, H. Xiao, S. Tian, H. Xie, G. Yang, N. Tsubaki, Y. Han, Y. Tan, Ternary copper-cobalt-cerium catalyst for the production of ethanol and higher alcohols through CO hydrogenation., App Catalysis A, 514 14 (2016).

[11] W. L. Roth, The magnetic structure of CO3O4., J. Phys. Chem. Sol., 25, 1 (1964).

[12] I. B. Krynetskii, B. A. Gizhevskii, S. V. Naumov, E. A. Kozlov, Size Effect of the Thermal Expansion of Nanostructural Copper Oxide., Fizika Tverdogo Tela, 50 723 (2008).

[13] T. Ivas, A. N. Grundy, E. Povoden-Karadeniz, L. J. Gaucklero, Phase diagram of CeO2-CoO for nano-sized powders., Calphad 36 57 (2012).

[14] H. Okamoto, Cerium-Cobalt Binary Alloy Phase Diagram., ASM Alloy Phase Diagrams Center 2 1047 (2007).

[15] W. Zhuang, Z. Y. Qiao, S. Wei, J. Shen, Thermodynamic evaluation of the Cu-R (R: Ce, Pr, Nd, Sm) binary systems., J. Phase Equilib. **17** 508 (1996).

[16] T. Nishizawa, K. Ishida, The Co-Cu (Cobalt-Copper) system., Bull. Alloy Phase Diagr. **5** 161 (1984).

[17] P. Knauth, G. Schwitzgebel, A. Tschöpe, S. Villain, Emf Measurements on Nanocrystalline Copper-Doped Ceria., J. Solid State Chem. **140** 295 (1998).

[18] M. Chen, B. Hallstedt, A. N. Grundy, , L. J. Gauckler, CeO_2-CoO Phase Diagram., J. Am. Ceram. Soc. **86** 1567 (2003).

[19] J. Marrero-Jerez, A. Murugan, I. S. Metcalfe, P. Núñez, TPR-TPD-TPO studies on CGO/NiO and CGO/CuO ceramics obtained from freeze- dried precursors., Ceram. Int. **40** 15175 (2014).

[20] A. Pintar, J. Batista, S. Hocevarz, TPR, TPO, and TPD examinations of $Cu_{0.15}Ce_{0.85}O_{2-y}$ mixed oxides prepared by co-precipitation, by the sol-gel peroxide route, and by citric acid-assisted synthesis., J. Colloid Interface Sci. **285** 218 (2005).

[21] L. Kundakovic, M. Flytzani-Stephanopoulos, Cu- and Ag-Modified Cerium Oxide Catalysts for Methane Oxidation., J. Catal. **179** 203 (1998).

[22] C.-W. Tang, C.-B. Wang, S.-H. Chien, Characterization of cobalt oxides studied by FT-IR, Raman, TPR and TG-MS., Thermochim. Acta **473** 68 (2008).

[23] P. Arnoldy, J. A. Moulijn, Temperature-programmed reduction of $CoOAl_2O_3$ catalysts., J. Catal. **93** 38 (1985).

[24] H. C. Yao, Y. F. Y. Yao, Ceria in automotive exhaust catalysts: I. Oxygen storage., J. Catal. **86** 254 (1984).

[24] N. K. Renuka, N. Harsha, T. Divya, Supercharged ceria quantum dots with exceptionally high oxygen buffer action., RSC Adv. **5** 38837 (2015).

[26] W. J. S. Schmid, R. Hausbrand, Cobalt oxide thin film low pressure metal-organic chemical

vapor deposition., Thin Solid Films **567** 8 (2014).

[27] L. E. Gómez, J. F. Múnera, B. M. Sollier, E. E. Miró, A. V. Boix, Raman in situ characterization of the species present in Co/CeO_2 and Co/ZrO_2 catalysts during the COPrOx reaction., Int. J. Hydrog. Energy **41** 4993 (2016).

[28] R. Berenguer, A. L. Rosa-Toro, C. Quijada, E. Morallón, Electrocatalytic oxidation of cyanide on copper-doped cobalt oxide electrodes., Appl. Catal. B **207** 286 (2017).

[29] M. J. Escudero, T. Rodrigo, L. Mendoza, M. Cassir, L. Daza, Porous nickel MCFC cathode coated by potentiostatically deposited cobalt oxide: I. A structural and morphological study., J. Power Sources **140** 81 (2005).

[30] A. Khana, C. Jiménez, O. Chaix-Pluchery, H. Roussel, J. L. Deschanvres, In-situ Raman spectroscopy and X-ray diffraction studies of the structural transformations leading to the $SrCu_2O_2$ phase from strontium-copper oxide thin films deposited by metalorganic chemical vapor deposition., Thin Solid Films **541** 136 (2013).

[31] G. Balakrishnan, C. M. Raghavan, C. Ghosh, R. Divakar, E. Mohandas, J. I. Song, S. I. Bae, T. G. Kim, X-ray diffraction, Raman and photoluminescence studies of nanocrystalline cerium oxide thin films., Ceram. Int. **39** 8327 (2013).

[32] T. R. Reina, S. Ivanova, O. H. Laguna, M. A. Centeno, J. A. Odrio- zola, WGS and CO-PrOx reactions using gold promoted copper-ceria catalysts: "Bulk CuO CeO_2 vs. CuO CeO_2/Al_2O_3 with low mixed oxide content"., App. Catal. **197** 62 (2016).

[33] B. M. Reddy, P. Bharali, G. Thrimurthulu, P. Saikia, L. Katta, S.-E. Park, Catalytic Efficiency of Ceria-Zirconia and Ceria-Hafnia Nanocomposite Oxides for Soot Oxidation., Catal. Lett. **123** 327 (2008).

[34] E. O. Jardim, S. Rico-Francés, F. Coloma, J. A. Anderson, E. V. Ramos-Fernandez, J. Silvestre-Alberoa, A. Sepúlveda-Escribano, Preferential oxidation of CO in excess of H_2 on Pt/CeO_2-Nb_2O_5 catalysts., Appl. Catal. A **492** 201 (2015).

[35] J. Llorca, P. R. D. L. Piscina, J.-A. Dalmon, N. Homs, Transformation of Co_3O_4 during ethanol steam reforming. Activation process for hydrogen production., Chem. Mater. **16** 3573 (2004).

[36] V. G. Hadjiev, M. N. Iliev, I. V. Vergilov, The Raman spectra of Co_3O_4., J. Phys. C **21** L199 (1988).

[37] J. F. Xu, W. Ji, X. Shen, W. S. Li, S. H. Tang, X. R. Ye, D. Z. Jia, X. Q. Xin, Raman Spectra of CuO Nanocrystals., J. Raman Spectrosc. **30** 413 (1999).

[38] J. Chrzanowske, J. C. Irwin, Raman Spectra from Cupric Oxide., Solid State Commun. **70** 11(1989).

[39] S.-I. Lee, K. Ahn, J. M. Vohs, R. J. Gorte, Cu-Co Bimetallic Anodes for Direct Utilization of Methane in SOFCs., Electrochem. Solid State Lett, **8** (1) A48 (2005).

[40] S.-I. Lee, J. M. Vohs, R. J. Gorte, A Study of SOFC Anodes Based on Cu-Ni and Cu-Co Bimetallics in CeO_2-YSZ., Journal of The Electrochemical Society, **151** (9) A1319 (2004).